Mathematical Biosciences and Engineering

http://www.aimspress.com/journal/mbe

MBE, 20(6): 11116–11138.
DOI: 10.3934/mbe.2023492
Received: 21 February 2023
Revised: 15 April 2023
Accepted: 17 April 2023
Published: 25 April 2023

Research article

Adaptive filter method in Bendlet domain for biological slice images

Yafei Liu[1], Linqiang Yang[1], Hongmei Ma[2] and Shuli Mei[1,*]

[1] College of Information and Electrical Engineering, China Agricultural University, Beijing 100083, China

[2] Yantai Research Institute, China Agricultural University, Yantai 264670, China

* **Correspondence:** E-mail: meishuli@cau.edu.cn.

Abstract: The biological cross-sectional images majorly consist of closed-loop structures, which are suitable to be represented by the second-order shearlet system with curvature (Bendlet). In this study, an adaptive filter method for preserving textures in the bendlet domain is proposed. The Bendlet system represents the original image as an image feature database based on image size and Bendlet parameters. This database can be divided into image high-frequency and low-frequency sub-bands separately. The low-frequency sub-bands adequately represent the closed-loop structure of the cross-sectional images and the high-frequency sub-bands accurately represent the detailed textural features of the images, which reflect the characteristics of Bendlet and can be effectively distinguished from the Shearlet system. The proposed method takes full advantage of this feature, then selects the appropriate thresholds based on the images' texture distribution characteristics in the database to eliminate noise. The locust slice images are taken as an example to test the proposed method. The experimental results show that the proposed method can significantly eliminate the low-level Gaussian noise and protect the image information compared with other popular denoising algorithms. The PSNR and SSIM obtained are better than other methods. The proposed algorithm can be effectively applied to other biological cross-sectional images.

Keywords: biological slice images; Bendlet; Shearlet; adaptive filter method; image denoising

1. Introduction

Biological slice images generally use biological tissues as raw materials. As one kind of biological cross-sectional image, it is an indispensable tool in biological histology. Biological slice images are widely used in biology, infectious diseases, pathology, and so on. It has crucial analytical value in the fields of quantification and measurement of biological tissue volumes and localization of pathologies. The biological slice images obtained under the microscope have rich closed-loop structures, the organs

and tissues represent smooth contours, and regular textures are included, which play an essential role in observing and analyzing the internal organizational structure of organisms. However, there is some noise in the process of gathering biological slice images [1]. For example, the camera sensor will generate a type of readout noise during charge readout due to circuit amplification or digital-to-analog conversion, etc., such noise appears in Gaussian distribution. The images also include a small number of other types of noise, such as salt-and-pepper noise, Poisson noise, etc. The histogram is shown in Figure 1(c). Tissue sections can also produce bright spots, noise, diffuse organs, and blurred tissue boundaries due to the infiltrated and stained material, which can affect further studies. Figure 1(a) reveals a kind of locust slice image, and Figure 1(b) shows fog-like noise on the image that blends with the locust texture, respectively.

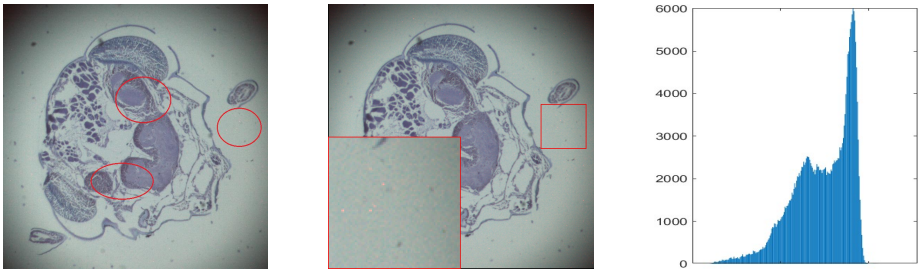

(a) (b) (c)

Figure 1. Contaminated image, (a) polluted image; (b) fog-like noise; (c) histogram of the target image.

Nowadays, domestic and foreign denoising algorithms emerge in an endless stream. In addition to the traditional denoising algorithms, such as average filtering, wiener filtering, total variation (TV) method [2], bilateral Filter [3], trilateral Filter [4], and compressed sensing (CS) [5], etc., there are also non-local means (NLM), side window filtering, block-matching and 3D filtering (BM3D), image denoising techniques based on deep learning and so on, new denoising algorithms combining various algorithms are also emerging. Non-local means filtering [6, 7] is a local-to-global filtering algorithm, which processes filtering based on similar blocks [8], and uses Gaussian weighted Euclidean distance to construct adaptive weights for similar blocks in the entire image, in order to perform filtering operation; BM3D [9] is another similar block-based filtering that is primarily divided into two steps: Basic estimation and final estimation. Basic estimation refers to dividing the image into several groups of self-similar blocks and combining them with collaborative filtering for processing. The final estimation is continued according to the original steps, but it will change the specific parameter value. Side window filtering [10] is a new edge-preserving filtering model proposed in 2019, which solves the problem that traditional filtering algorithms cannot preserve edges effectively. Currently, the convolutional neural network VGGNet [11], GoogLeNet [12], residual network ResNet [13, 14], generative adversarial network GAN [15] and graph neural network GNN [16] in deep learning, etc., all have good applications in image denoising.

At present, hybrid image denoising algorithms combining multiple algorithms are also emerging. For example, the multi-scale geometric analysis method combined with other classic algorithms [17, 18], and the improved image denoising algorithm for deep learning algorithm [19–21]. The denoising capability of deep learning-related algorithms is easily limited by data sets, hardware

resources, and running time [22]. Slice images will not only generate noise during the acquisition process of microscopy equipment but also the generated noises may be integrated with the image information. It is easy to damage the texture when removing noise, and easy to produce noise residue when protecting the texture correspondingly. Most filtering methods also do not take into full account the unique closed-loop structural characteristics of biological slice images. Therefore, in order to adapt to the image texture structure, this study uses bendlets in the multiscale geometric analysis method to conduct experiments.

The multi-scale geometric analysis tool [23] developed in recent years can optimally approximate the geometric structure of high-dimensional data such as images [24]. It could effectively solve the problem that traditional denoising algorithms cannot effectively protect image texture. The existing multi-scale geometric analysis methods are Wedgelet [25, 26], Beamlet [27], Ridgelet [28], Curvelet [29, 30], Bandelet [31, 32], Contourlet [33], Shearlet [34, 35], Bendlet [36, 37] and so on. In this regard, Bendlets is the latest multiscale geometric analysis method proposed by Lessig et al. It is a second-order Shearlet system, which overcomes the deficiency of first-order Shearlet in approximating curve textures. As a new type of multi-dimensional function approximation method, Shearlet has strong directional sensitivity and sparse representation performance. Therefore, it has better effects than current methods such as Wedgelet, Beamlet, Ridgelet, Curvelet, Bandelet [38, 39], Contourlet and so on, so Bendlet has state-of-the-art performance [40]. One image is decomposed into different coefficients by the Bendlet system with specific scale, orientation, and curvature parameters [41], and the coefficients can compose a dataset of image features. After that, we can perform operations such as image registration, denoising, restoration, etc.

This study is organized as follows: Section 2 briefly introduces the basic flow of the algorithm of this paper; Section 3 elaborates on the application of bendlets in image representation and the implementation of adaptive filters; Section 4 analyses in detail the processing effect of this study on different biological slice images; Finally, Section 5 gives some concluding remarks of this paper.

2. Methods

In this paper, we present a denoising algorithm based on the Bendlet transform, as illustrated in Figure 2 [42]. The proposed method consists of the following main steps: First, acquire an image feature database object based on the different directions or orientations defined by the Bendlet system. This system allows for precise boundary curve detection and texture feature identification of the target image; Then, an adaptive threshold is used to represent each object of the image feature database, sparsely. The target image contains raw noise in the production process and uneven texture caused by tool cutting. We first normalize Bendlets for better comparability and construct the index set of Bendlets. Combine the Bendlet system with a threshold correction to approximate each object's edge and texture, effectively filtering noise and repairing damaged textures; Finally, reconstruct the resulting image by the inverse bendlet system. Evaluate the denoising effect using the image quality evaluation index and colormap.

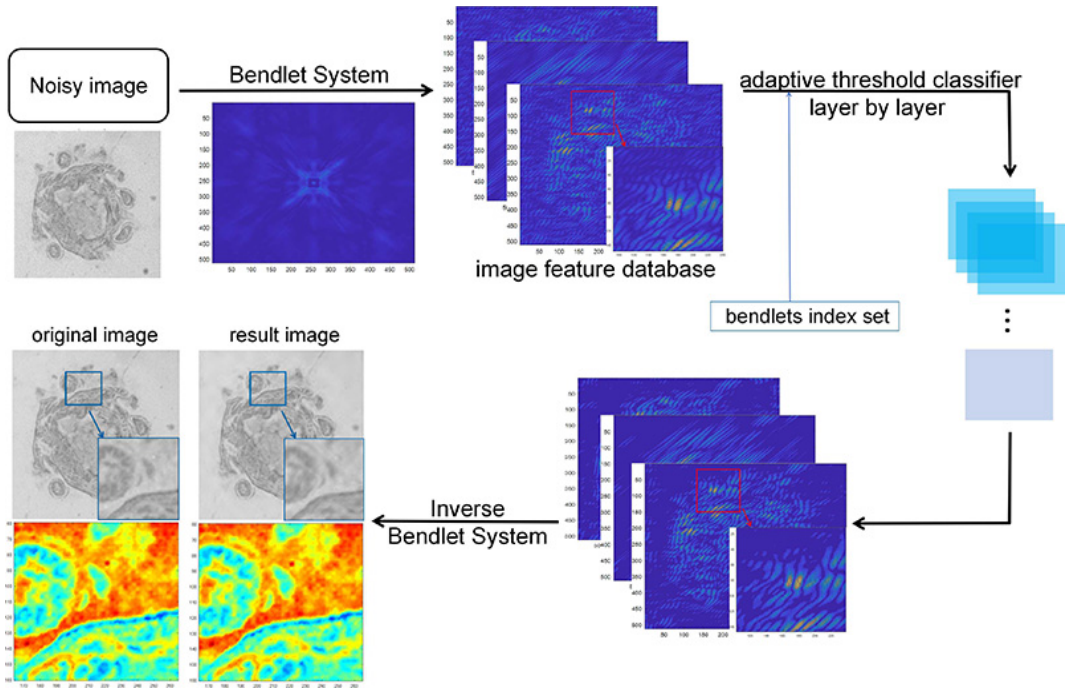

Figure 2. The framework of the proposed method.

3. Materials and detailed scheme

3.1. Construct image feature database

The Bendlet system represents the original image as an image feature database based on the image size and Bendlet parameters, and this database can be divided into image high-frequency and low-frequency sub-bands. This paper proposes an algorithm that fully utilizes the Bendlet representation characteristics of high and low-frequency information. It subdivides the sub-images in the image feature dataset and selects the corresponding thresholds based on their texture distribution characteristics to perform the denoising process.

3.1.1. Bendlet transform

Shearlet is highly efficient at extracting and characterizing boundary curves in piecewise smooth images, detecting corner points, and analyzing their properties compared to other directional representation systems. However, shearlet cannot classify curvature, which still has shortcomings in the analysis of images' texture properties [36]. In contrast, the Bendlet system (BS) addresses this deficiency and simplifies the directional representation form of the Shearlet system (SH).

The continuous Bendlets transform of function $f(x)$ is as follows:

$$BS_{\psi}^{(\alpha)} := SH_{\psi}^{(2,\alpha)} = \left\{\psi_{a,s,b,t} | (a,s,b,t) \in S^{(2,\alpha)}\right\} \tag{3.1}$$

where $\psi_{a,s,b,t} := \pi^{(2,\alpha)}(a,s,b,t)\psi$, when $(a,s,b,t) \in S^{(2,\alpha)}$,

$$BS_{\psi}^{(\alpha)}(f)(a,s,b,t) := SH_{\psi}^{(2,\alpha)}(f)(a,s,b,t) = \langle f, \psi_{a,s,b,t} \rangle \tag{3.2}$$

The scale, shear, bend, and translation parameters are denoted a, s, b & t, respectively. The Eq (3.3) is used to calculate the curvature.

$$K = \frac{2\left|b'\right|}{(1 + (s')^2)^{(3/2)}} \tag{3.3}$$

For each $a > 0 \,\&\, a \in [0, 1]$, A is an anisotropic matrix which is defined as $A_{a,\alpha} := \left(\begin{smallmatrix} a & 0 \\ 0 & a^{\alpha} \end{smallmatrix}\right)$, replacing the parabolic scaling in the Shearlet system with this α scaling method [43], allows Bendlet's decay rate [44] to provide more precise curvature and orientation for different areas of the image [45].

As shown in Figures 3 and 4, For each $a \to 0$, $BS_{\psi}^{(\alpha)}(f)(a, s, b, t)$ approaches different scenes of the image texture structure [46].

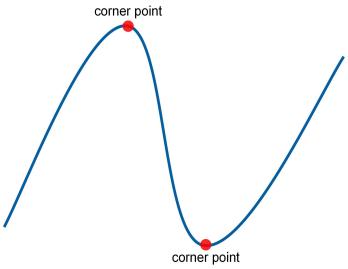

Figure 3. Smooth curve.

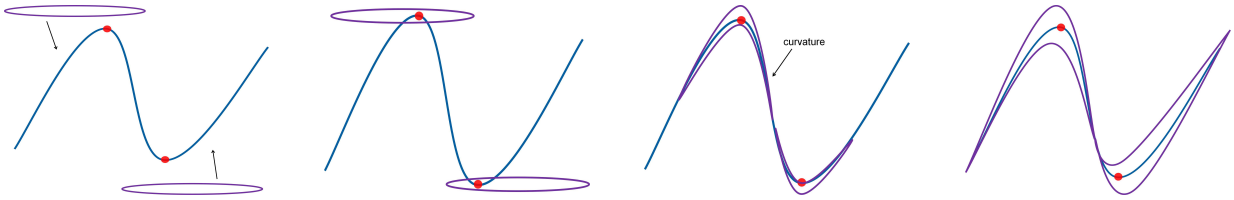

Figure 4. $a \to 0$, different approximation scenarios of $BS_{\psi}^{(\alpha)}(f)(a, s, b, t)$.

Suppose the boundary is ∂D,

a) $t \notin \partial D$, $BS_{\psi}^{(\alpha)}(f)(a, s, b, t)$;

b) $t \in \partial D$, the BT function $BS_{\psi}^{(\alpha)}(f)(a, s, b, t)$ continue to perform staggered transformation through different shear parameters s and bending parameters b, and select the value with the slowest decay when $a \to 0$, $BS_{\psi}^{(\alpha)}(f)(a, s, b, t) <= 0$;

c) $t \in \partial D$, The shear parameter s corresponds to the boundary t [47], but the bending parameter b is not satisfied, $BS_{\psi}^{(\alpha)}(f)(a, s, b, t)$ will show a medium value;

d) $t \in \partial D$, both the shear and bend parameters $s\&b$ correspond to the boundary t, and $BS_{\psi}^{(\alpha)}(f)(a, s, b, t)$ will show a higher coefficient value [37].

Shearlet uses the Meyer wavelet as the basis function, but the convergence speed of the Meyer wavelet is very fast. The Daubechies8 wavelet has a longer vanishing moment, which is smoother than the Meyer wavelet, and has an optimal effect when approximating the image. Figure 5 is the Meyer wavelet and Figure 6 is the Daubechies8 wavelet, respectively.

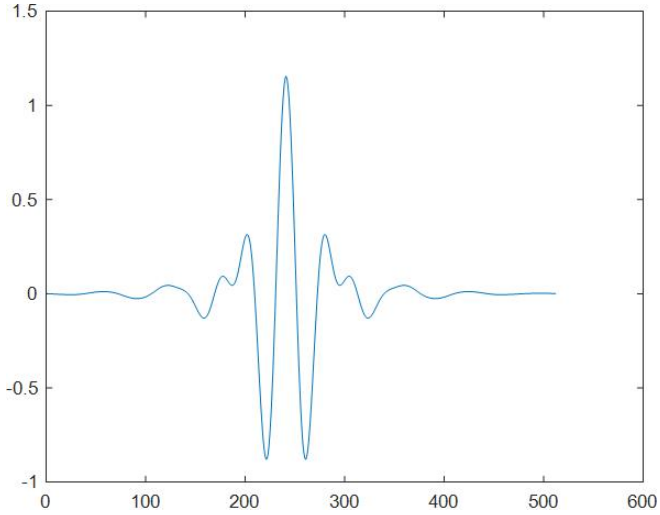

Figure 5. Meyer wavelet.

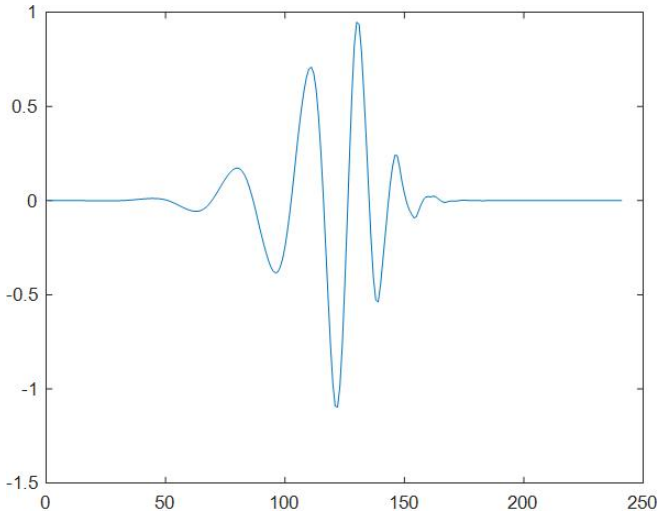

Figure 6. Daubechies8 wavelet.

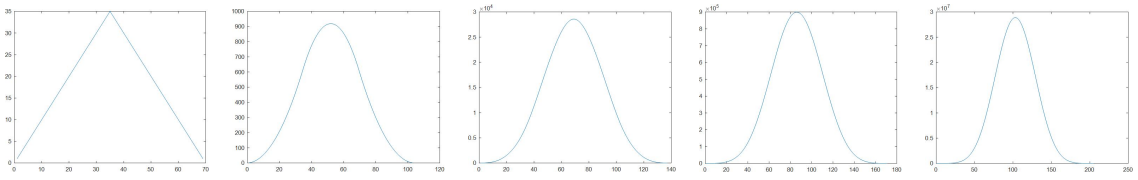

(a) (b) (c) (d) (e)

Figure 7. Five different types of low-pass filters.

The Bendlet system is comprised of high-pass and low-pass filters. The low-pass filter is defined by a separable generator with B-spline properties, as depicted in Figure 7. On the other hand, the high-pass filters are constructed using a Daubechies8 wavelet transform, which is shown in Figure 8(c).

The Daubechies8 wavelet, which is one of the bending elements of the Bendlet system, is the bending element [1, 1, 0, 0]. These four numbers correspond to the cone, scale, shear, and bending parameters of the Bendlet system, separately. By applying the Bendlet bending stagger transformation matrix to Figure 8(a), we obtain Figure 9. Figure 9(b) presents a top view of the transformed Daubechies8 wavelet, which is also one of the bending elements of the Bendlet system, is the bending element [1, 1, 1, -1]. Notably, the 'cone' parameter is further divided into a horizontal and a vertical cone.

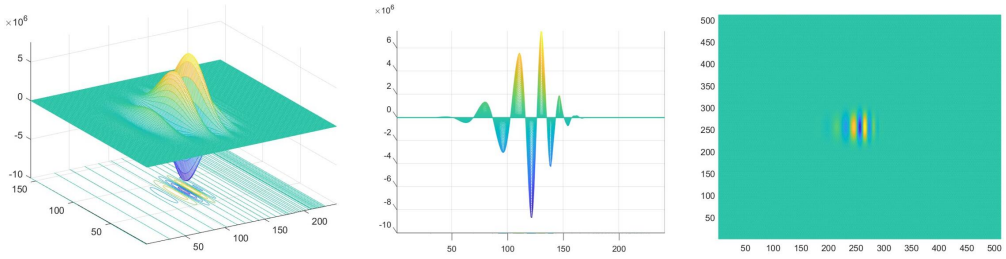

(a) (b) (c)

Figure 8. 3D representation of Daubechies8, (a) 3D surface plot of Daubechies8, (b) Sectional view of Daubechies8, (c) Top view of Daubechies8.

3.1.2. Image representation based on Bendlet system

According to the above method, each direction element of the bendlet and the corresponding biological slice image features are shown in Figure 10. The original image is first Fourier transformed to obtain the centralized spectrogram, and then the frequency domain image is convolved with the Bendlet coefficients and later converted to the time domain, thus completing the Bendlet decomposition operation of the image, as shown in Figure 10(c).

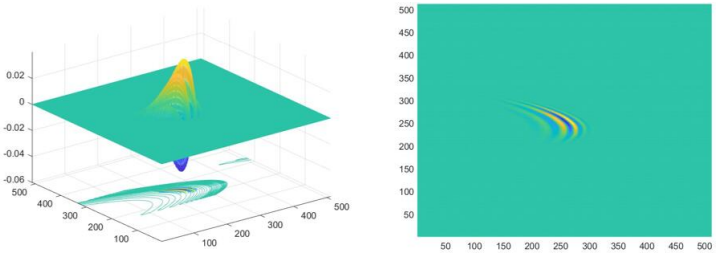

(a) (b)

Figure 9. A transformed Daubechies8 wavelet, (a) 3D representation of the transformed Daubechies8, (b) Top view of the transformed Daubechies8.

Figure 10(a),(b) illustrates the high-frequency components of the bendlet, which are constructed by high-pass filters. Figure 10(c) is the high-frequency coefficient of the corresponding original image, which captures the detailed information of the target image. In contrast, the low-frequency component of the bendlet is represented by a single '0', which is [0,0,0,0], as shown in Figure 11(a). The low-frequency coefficient of the target image is shown in Figure 11(b),(c), which only reflects the image contour information. Figure 11(d) shows the Shearlet low-frequency component. Figure 11(e),(f) shows the low-frequency information obtained after processing by the Shearlet system. We can see that Figure 11(b) contains not only the contour information of the image, but also part of the image

detail texture, it is a high-frequency signal, which also contains the noise we need to remove, so there is a problem of incomplete noise reduction. Correspondingly, the high-frequency information in Figures 10 and 11(b) constitute the image feature dataset obtained by Bendlet processing. There is only one low-frequency image, while the high-frequency image is related to the predefined Bendlet parameter. The larger the value of the Bendlet parameter, the greater the number of high-frequency sub-bands and the greater the number of images in the image feature dataset.

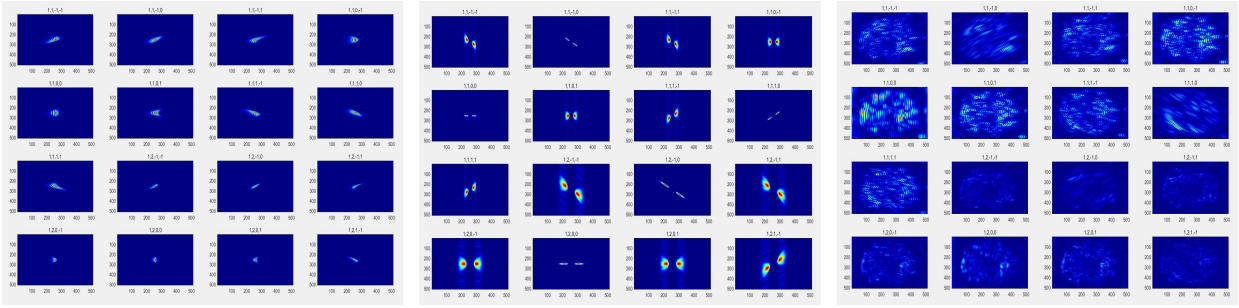

(a) (b) (c)

Figure 10. Bendlet elements of spatial and frequency distributions and their use to represent biological slice images, (a) Some bendlet elements in the spatial domain, (b) Some bendlet elements in the frequency domain, (c) Presentation of some Bendlet coefficients for biological slice image.

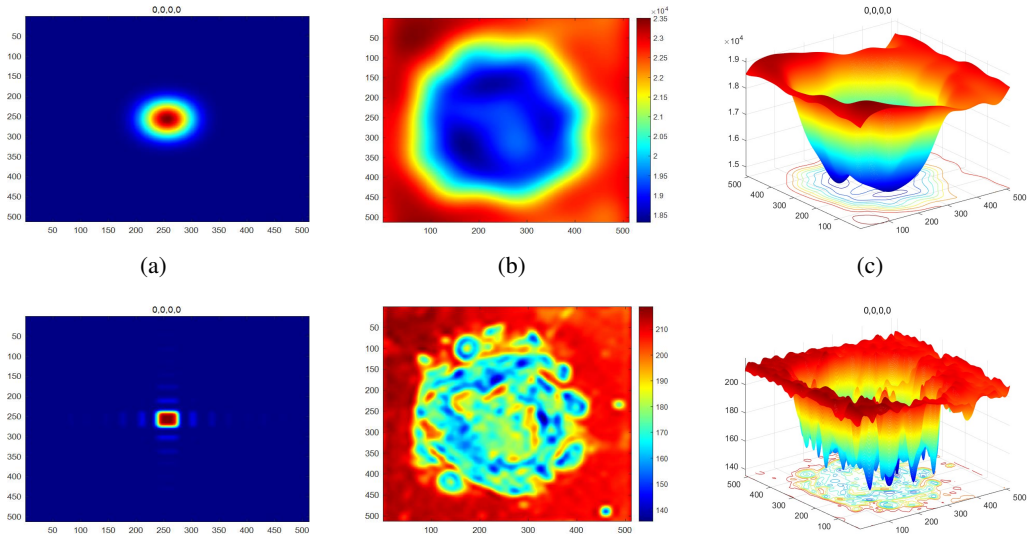

(a) (b) (c)

(d) (e) (f)

Figure 11. The low-frequency information of the original image. (a) Bendlet low-frequency component; (b) Low-frequency information after Bendlet processing; (c) 3D surface plot of 'b'; (d) Shearlet low-frequency component; (e) Low-frequency information after Shearlet processing; (f) 3D surface plot of 'e'.

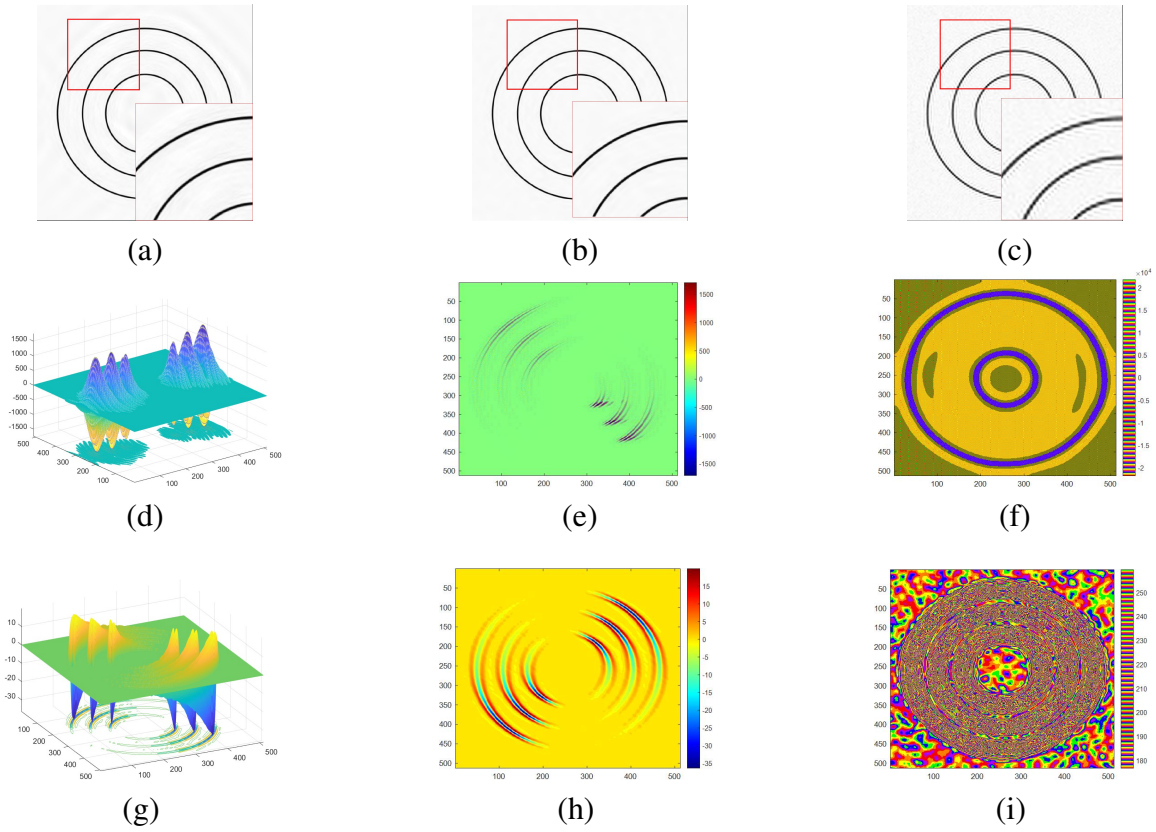

Figure 12. Results of Bendlet, Shearlet, and Daubechies8 wavelet processing of concentric circle images. (a) Bendlet processed, (b) Shearlet processed, (c) Daubechies8 wavelet processed, (d) Coefficient distribution of Bendlet in direction 5, (e) High-frequency coefficient distribution of Bendlet in direction 1, (f) Low-frequency coefficient distribution of Bendlet, (g) Coefficient distribution of Shearlet in direction 5, (h) High-frequency coefficient distribution of Shearlet in direction 1, (i) Low-frequency coefficient distribution of Shearlet.

We look further at the edge-preserving properties of Bendlet in conjunction with concentric circle images. Figure 12 shows the results of adding Gaussian noise of intensity 15 to the concentric circle image. Based on the processing results of Bendlet, Shearlet, and Daubechies8 wavelet for noisy images, as shown in Figure 12(a)–(c), there is little difference in the denoising effect of Bendlet and Shearlet from a visual perspective only, both of which are stronger than conventional wavelets. There are also fewer artificial artifacts in the reconstruction process. From the prism colormap, as shown in Figure 12(f),(i), we can see that the low-frequency image of Shearlet contains the image contour and also contains a more detailed texture. According to the principle of wavelet decomposition denoising, the noisy image is decomposed into high-frequency and low-frequency information, and the purpose of denoising is achieved by retaining the low-frequency information of the image and removing the high-frequency information, therefore, the low-frequency information of the processed image after the Daubechies8 wavelet also contains both contour and detailed texture information. Bendlet, on the other hand, contains only the contour information, so Bendlet can ensure that the edges of the ring structure are precise in the process of denoising. Precisely because Bendlet has an additional bending parameter compared to Shearlet, it is more sensitive to the curved texture of the image, so the presentation of

Bendlet is relatively complex compared to the high-frequency image obtained using Shearlet, as shown in Figure 12(e),(h). Figure 12(d),(g) further verifies that there is no image contour information in the Bendlet high-frequency coefficients, whereas, in the Shearlet high-frequency coefficients, the 3D grid map shows the numerical values of image edges as 0, thus illustrating that the Shearlet high-frequency coefficients also contain image contour information. In summary, the Shearlet transform can preserve the image texture structure better but is a little less effective in preserving edges.

3.2. Construct adaptive filter

This study has combined the characteristics of Bendlets outlined above with the results of image representation. Using this information, the study has constructed an adaptive filter based on the Bendlet index set. The aim is to protect image edges while retaining the maximum effective detail texture of the image for denoising purposes.

The result of normalizing the Bendlet element using the L2-norm is displayed in Figure 13. Next, the Bendlet index set is utilized to correct the target image layer by layer. The paper proposes a threshold function as follows:

$$C(i,j)^{'} = \begin{cases} C(i,j), & C(i,j) > T \\ 0, & else \end{cases} \tag{3.4}$$

$$T = \frac{\sigma BT_N Med|C(i,j)|}{K} * \lambda \tag{3.5}$$

$$K = \sqrt{max((\overline{C(i,j)} - Med|C(i,j)|), 0)} \tag{3.6}$$

where $C(i,j)$ and $C(i,j)^{'}$ represent the sub-images before and after denoising, respectively. Unlike traditional threshold denoising algorithms, this study adaptively selects thresholds based on the Bendlet index set and noise intensity. BT_N represents the normalized bendlet elements, σ refers to the simulated noise intensity. Since the noise of the microscopic images presents a Gaussian distribution, here is the Gaussian noise intensity value. Since the bendlet index contains four variables, which are cone, scale, shear, and bending. According to the bendlet system establishment rules, bendlets are divided into a horizontal cone and a vertical cone. The corresponding bendlet elements are generated according to the predefined scale, shear and bending number in each cone. Finally, a low-frequency element is generated outside both cones. This study sequentially extracts sub-band coefficients in both horizontal and vertical cones, sub-band images with the same shear and bending coefficients were individually grouped, calculate the median and mean values of the corresponding coefficients. The value of λ is a constant, which is taken as 1.37 in this paper by experimental test.

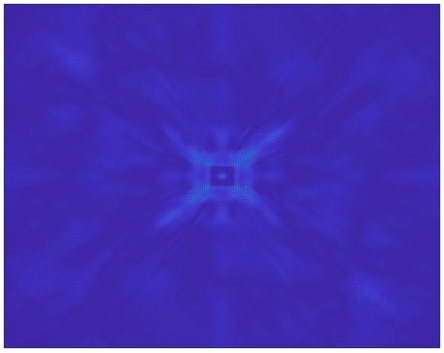

Figure 13. Normalized bendlet system.

The Bendlet transform separates an image into high-frequency and low-frequency components, with the latter carrying most of the contour information. To preserve these edges, the denoising algorithm presented in this paper applies thresholding only to the high-frequency component, leaving the low-frequency component untouched. This approach effectively removes noise from the image while maintaining its important features.

4. Experimental results and analysis

To demonstrate the effectiveness of our proposed algorithm, we conducted experiments using locust slice images and compared its performance with five other image processing methods, namely Shearlet, Total variation (TV) method, Bilateral Filter, Trilateral Filter, and Compressed Sensing (CS). We used Peak Signal to Noise Ratio (PSNR) and Structural Similarity Index Measure (SSIM) as evaluation metrics for the algorithms' performance. Table 1 summarizes the results of the experiments.

Furthermore, we present the image processing results of each algorithm for images (1)–(5) with a Gaussian noise level of 10 in grayscale and jet color map formats. These results are shown in Figures 14 and 15.

Table 1. Image denoising effect comparison for different algorithms.

Image	Noise Level	Metrics	Noisy Image	Proposed Method	Shearlet Method	TV Method	Trilateral Filter	Bilateral Filter	CS Method
(a)	10%	PSNR	21.9207	**36.7813**	35.7802	32.8169	34.5964	34.4396	32.4981
		SSIM	0.52824	**0.9278**	0.91233	0.85737	0.86983	0.86343	0.76884
	20%	PSNR	19.5721	**33.004**	32.8853	31.6295	29.2904	26.6472	27.7441
		SSIM	0.26576	**0.88346**	0.87365	0.82753	0.66341	0.51961	0.51184
	30%	PSNR	17.4048	30.7488	**30.8472**	27.9407	25.7795	21.1166	24.5389
		SSIM	0.15925	**0.8471**	0.84254	0.63996	0.4945	0.26981	0.15925
	80%	PSNR	11.7259	25.5044	**26.1508**	16.3857	16.1316	11.7401	17.3293
		SSIM	0.03987	**0.73986**	0.73753	0.10697	0.12982	0.040677	0.10906

Continued on next page

Image	Noise Level	Metrics	Noisy Image	Proposed Method	Shearlet Method	TV Method	Trilateral Filter	Bilateral Filter	CS Method
(b)	10%	PSNR	21.9071	**36.8856**	35.9801	32.4617	34.3966	34.2577	32.5344
		SSIM	0.52967	**0.92926**	0.91362	0.85618	0.87251	0.86665	0.76906
	20%	PSNR	19.5873	**33.0774**	33.0045	31.3629	29.1928	26.5882	27.7516
		SSIM	0.26701	**0.88656**	0.87771	0.82847	0.67161	0.53131	0.51422
	30%	PSNR	17.4752	30.7605	**30.8957**	27.7721	25.7628	21.1256	24.545
		SSIM	0.16272	**0.85132**	0.81666	0.64574	0.50542	0.28233	0.35355
	80%	PSNR	11.7878	25.064	**25.8322**	16.5496	16.2766	11.8328	17.3778
		SSIM	0.03969	**0.74578**	0.74195	0.11259	0.13459	0.042209	0.11212
(c)	10%	PSNR	21.9195	**36.9422**	36.519	33.2824	34.9469	34.7304	32.6423
		SSIM	0.52872	**0.92745**	0.91971	0.86004	0.87297	0.86579	0.77115
	20%	PSNR	19.5794	**33.2452**	32.8587	32.0063	29.4637	26.7245	27.7938
		SSIM	0.26381	**0.88613**	0.86072	0.83042	0.66676	0.51718	0.51469
	30%	PSNR	17.391	**31.1362**	31.1136	28.0379	25.8319	21.1138	24.5674
		SSIM	0.15786	**0.8524**	0.81504	0.63916	0.48907	0.25812	0.35315
	80%	PSNR	11.597	25.5893	**26.4272**	16.3732	16.0997	11.6975	17.3254
		SSIM	0.03802	**0.74243**	0.74231	0.10796	0.127	0.040014	0.10845
(d)	10%	PSNR	21.9013	**37.0325**	36.0778	33.9669	35.2195	34.945	32.7339
		SSIM	0.52502	**0.92795**	0.9139	0.87484	0.87224	0.86381	0.77026
	20%	PSNR	19.598	**33.3204**	33.0155	32.5117	29.5126	26.7516	27.811
		SSIM	0.2611	**0.887**	0.87922	0.84246	0.66156	0.50793	0.51191
	30%	PSNR	17.4164	31.0547	**31.2635**	28.1648	25.9036	21.1221	24.5774
		SSIM	0.15547	**0.85546**	0.81838	0.63865	0.48568	0.25036	0.35037
	80%	PSNR	11.7026	25.5024	**26.3299**	16.4162	16.1419	11.7365	17.325
		SSIM	0.03796	**0.75477**	0.74822	0.10592	0.12811	0.038835	0.10712
(e)	10%	PSNR	21.916	**37.4656**	36.1373	33.6002	35.102	34.8316	32.6722
		SSIM	0.56206	**0.94068**	0.9297	0.87688	0.87917	0.87103	0.78814
	20%	PSNR	19.5904	**33.2002**	32.7128	32.223	29.4893	26.7242	27.8318
		SSIM	0.29364	**0.89113**	0.86286	0.8463	0.67608	0.52577	0.54875
	30%	PSNR	17.4331	30.5355	**30.8348**	28.077	25.8694	21.1116	24.6065
		SSIM	0.17849	**0.85024**	0.81635	0.65087	0.50318	0.26886	0.38819
	80%	PSNR	11.7069	24.5636	**25.6379**	16.4038	16.2139	11.7541	17.3559
		SSIM	0.04358	0.7159	**0.71995**	0.12337	0.15265	0.044933	0.12378

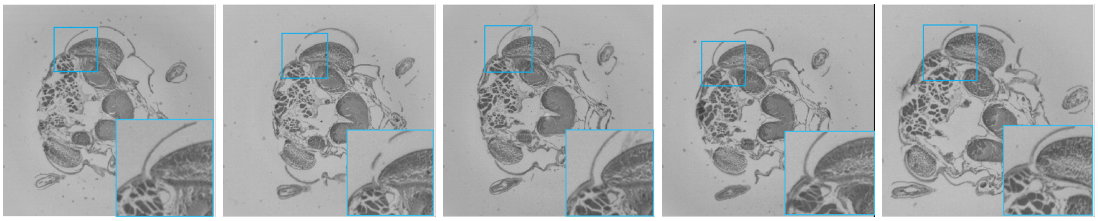

(a)

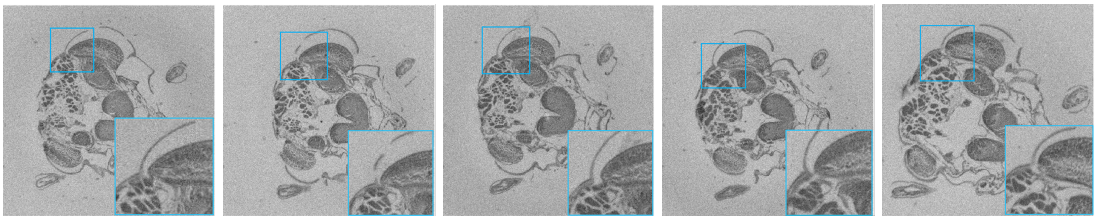

(b)

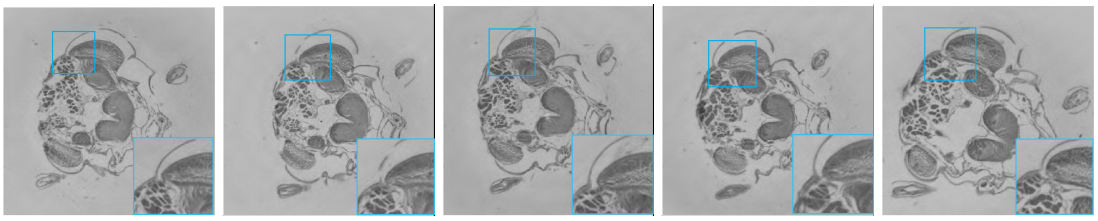

(c)

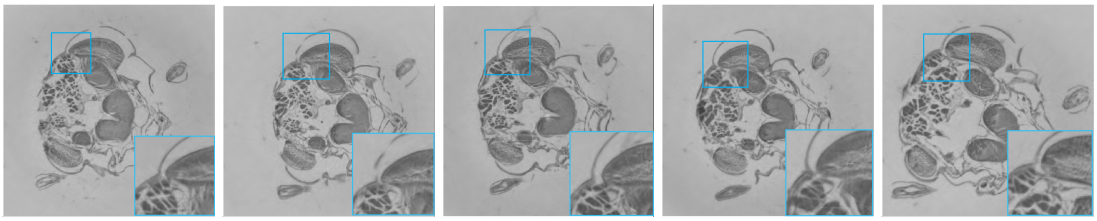

(d)

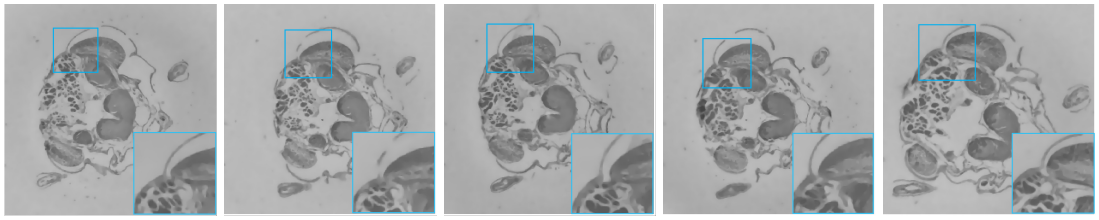

(e)

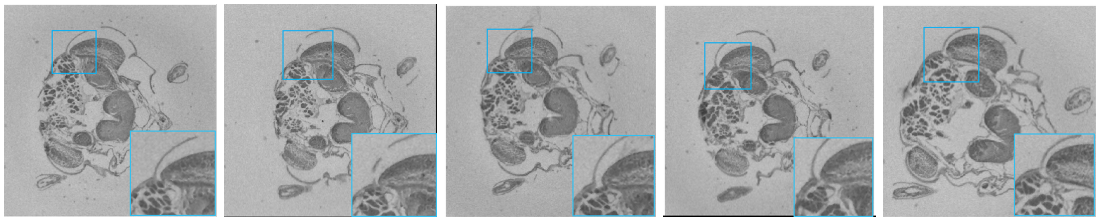

(f)

Continued on next page

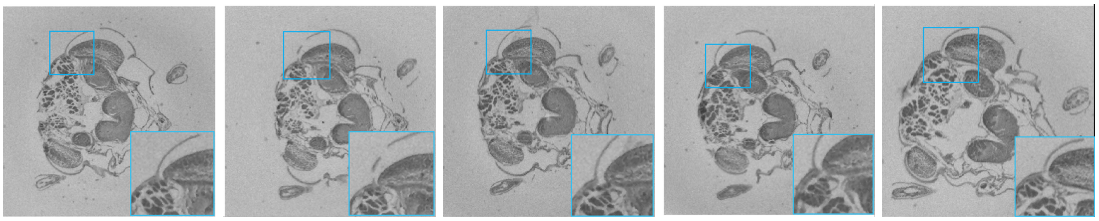

(g)

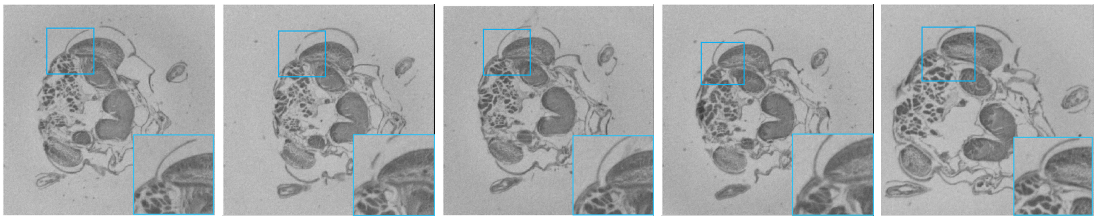

(h)

Figure 14. Gray and jet colormap of the locust slice images, (a) Original image, (b) Noisy image, (c) Proposed method, (d) Shearlet method, (e) TV method, (f) Trilateral Filtering, (g) Bilateral Filtering, (h) Compressed sensing.

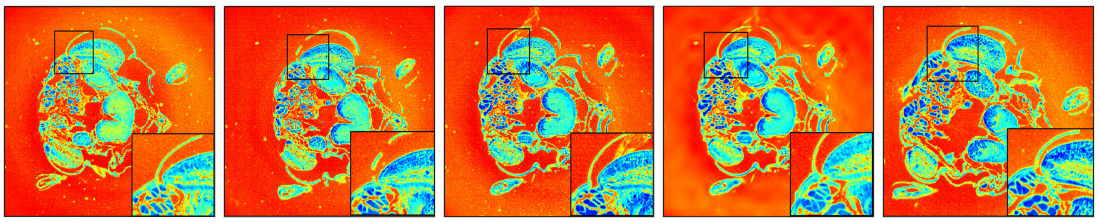

(a)

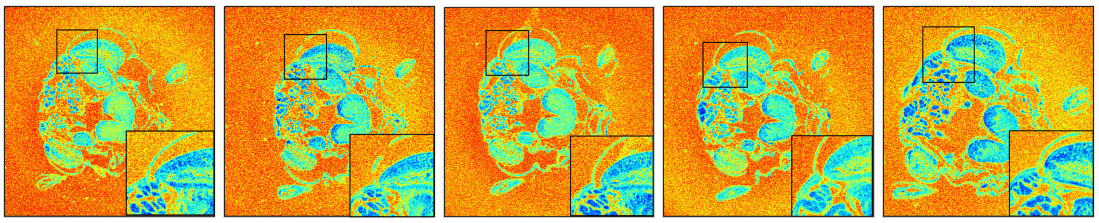

(b)

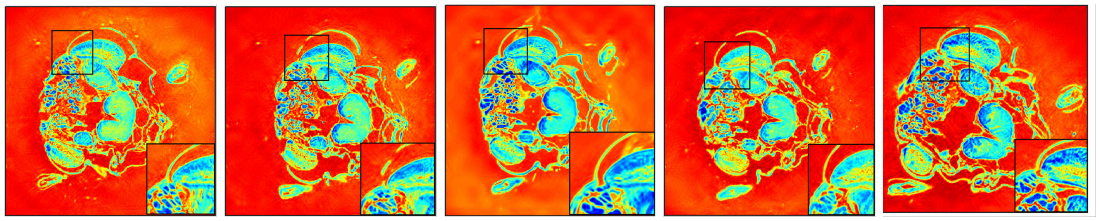

(c)

Continued on next page

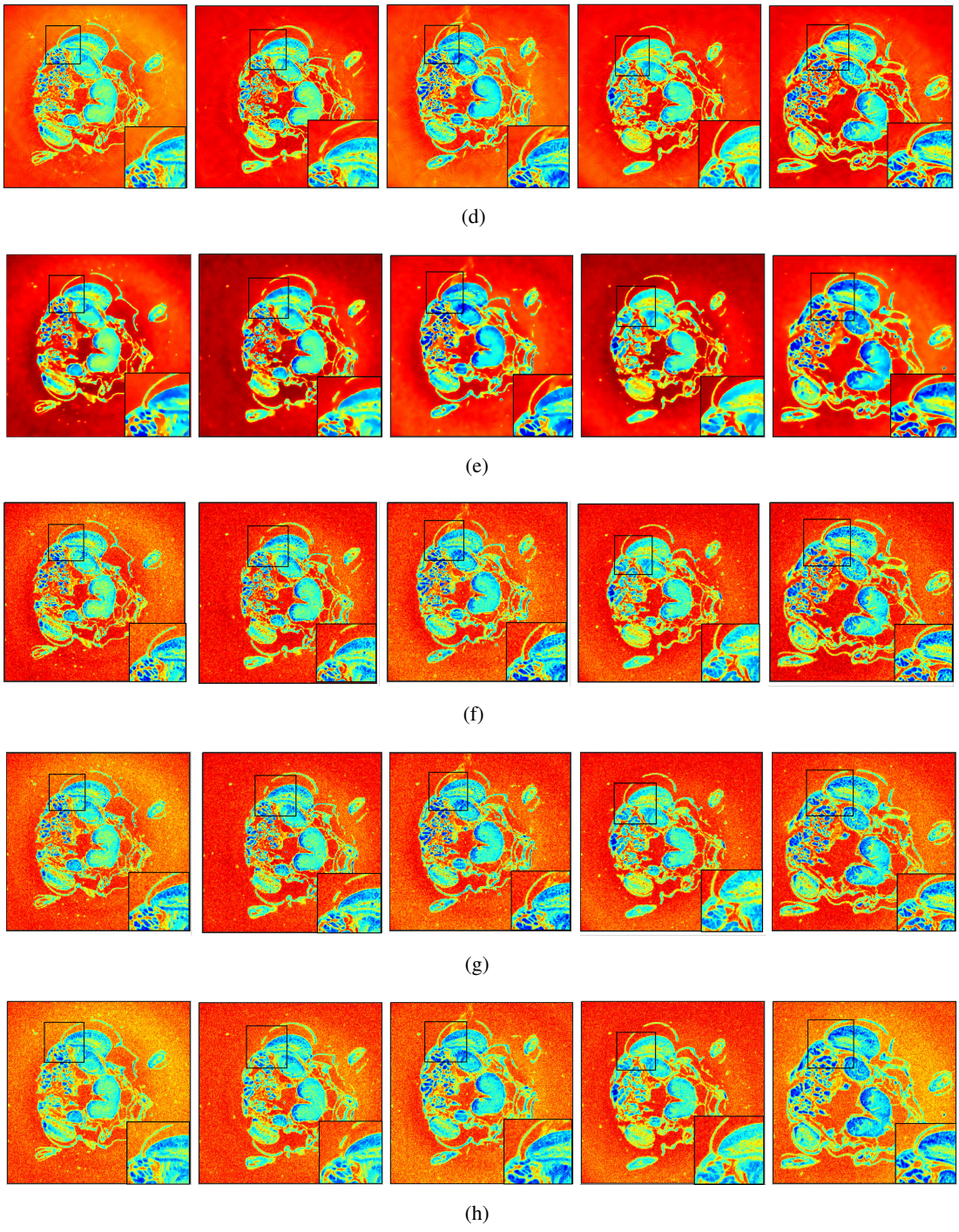

Figure 15. Jet colormap of the locust slice images, (a) Original image, (b) Noisy image, (c) Proposed method, (d) Shearlet method, (e) TV method, (f) Trilateral Filtering, (g) Bilateral Filtering, (h) Compressed sensing.

To further demonstrate the effectiveness of the algorithm in this paper, the method we proposed is compared with the adaptive and multi-threshold image denoising algorithm [22], hard thresholding, soft thresholding [48], the non-negative garrote (NNG) function [49], the smoothly clipped absolute deviation (SCAD) function [49], and the sigmoidal shrinkage function [50], and the denoising results are shown in Table 2.

Table 2. Image denoising effect comparison.

Image	Noise Level	Metrics	Proposed Method	[22] Method	Hard Thresholding	Soft Thresholding	NNG Function	SCAD Function	Sigmoid Function
(a)	10%	PSNR	**36.7813**	36.1527	34.793	30.6563	29.3368	13.5386	34.7605
		SSIM	**0.9278**	0.91913	0.90762	0.8582	0.83063	0.81283	0.90726
	20%	PSNR	**33.004**	32.998	31.2246	27.8204	27.1953	13.4906	31.1898
		SSIM	**0.88346**	0.8731	0.85649	0.7995	0.77972	0.69663	0.85601
	30%	PSNR	**30.7488**	30.2377	29.1769	26.8446	26.2135	13.4244	29.0919
		SSIM	**0.8471**	0.8358	0.81964	0.76966	0.75788	0.58208	0.8183
	80%	PSNR	25.5044	**25.8586**	24.805	23.7265	22.6912	12.6506	24.8787
		SSIM	0.74229	**0.75638**	0.74026	0.73499	0.73346	0.35344	0.74024

From Table 1, we can observe the quantitative results of these six algorithms for different types of biological slice images. Images (1)–(5) correspond to the five images of Figure 14(a), respectively. From a macro perspective, the effect of the image denoising algorithm based on bendlet and shearlet is relatively good, but bendlet is slightly less effective when dealing with high noise intensities. Among the algorithms involved in Table 1, the algorithms with better noise reduction effects are in the following order: Total variation, Trilateral filter, Bilateral filter, and Compressed sensing.

Combined with the operation effect of Figures 14 and 15, we can see that the above six algorithms can effectively remove Gaussian noise, but the ability to denoising is slightly different. The algorithm proposed in this paper can not only remove the noise but also the redundant noise in the original image. It also has the effect of image enhancement while denoising, which can better preserve the texture details in the image. The shearlet method is slightly inferior to the bendlet method, and it can also protect the texture of the image to a certain extent; the total variation and compressed sensing method will damage image details while denoising; bilateral filtering and trilateral filtering can preserve image details well, but there are still some noises not completely removed. Among them, the total variation method will over smooth the image when the noise intensity is very low but will achieve a better denoising effect than trilateral filtering when the noise intensity is average.

From Table 2, we can observe the quantitative results of the Bendlet transform using these seven thresholds in Figure 14(a1). We can see that the algorithm in this paper slightly outperforms the adaptive and multi-threshold image noise reduction algorithm proposed in [22]. Bendlet transform in the process of using other threshold functions, the denoising effects are in the following order: hard thresholding, the sigmoidal shrinkage function, soft thresholding, and the non-negative garrote (NNG) function, and poor denoising effect with the smoothly clipped absolute deviation (SCAD) function.

Since the bendlet system has one more bending parameter than the shearlet system, the number of image directions and decomposition layers to be processed is more, so the images will be slightly rough compared with the images processed by shearlet. But according to the numerical evaluation indexes, this doesn't affect its ability. What's more, the bending parameters in the bendlet system can optimally approximate the curved texture of the slice image relative to the shearlet system, which has a certain repairing effect on slight image damage. And the lower level of noise and bendlet-like artifacts [51, 52] are similar to the damage of part of the image information. Therefore, the bendlet system can better restore the image details and remove noise in biological cross-section images to a certain extent. However, when the noise level is high, the bending parameter can produce more artifacts, which could interfere with the image and affect the filtering effect.

As shown in Figure 16, since the microsection needs to be made of liquid medicine, during the imaging process, air bubbles and image folds will interfere with the image texture, and the image texture will also be affected by the liquid soaked. After bendlet processing, combined with the jet colormap of the original image and the resulting image, we can see that the bendlet enhances the details of the image, effectively removes the noise in the image, and inpainting small damage in the image. So, bendlets also have a significant effect on image enhancement and small breakage removal.

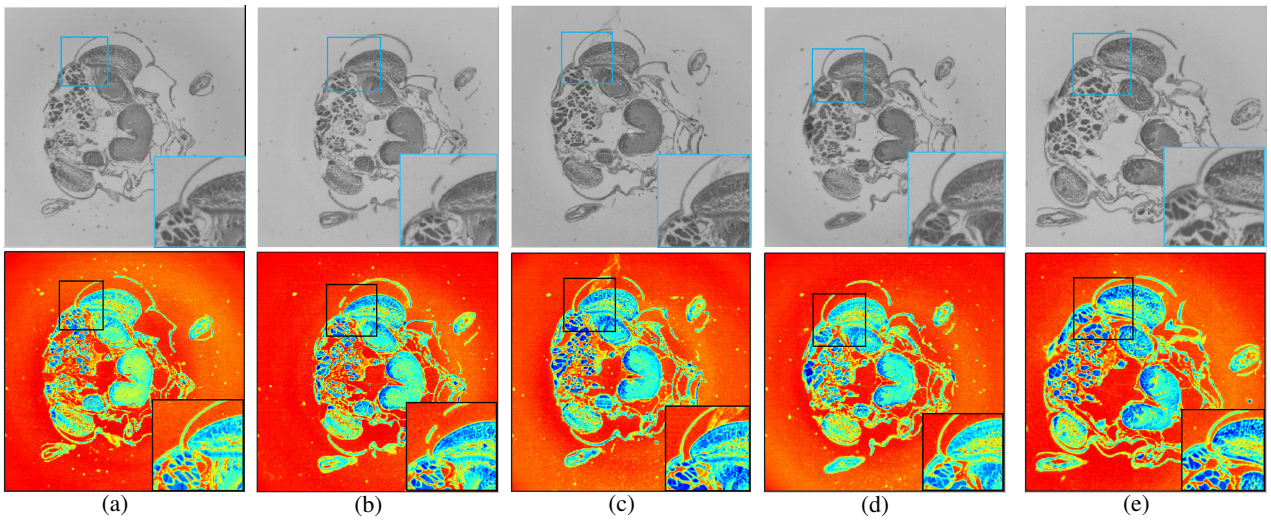

Figure 16. The effect of bendlet on image enhancement, (a) PSNR: 51.6792 dB, SSIM: 0.99354 dB, (b) PSNR: 51.5949 dB, SSIM: 0.99343 dB, (c) PSNR: 51.6341 dB, SSIM: 0.99354 dB, (d) PSNR: 51.6194 dB, SSIM: 0.9935 dB, (e) PSNR: 51.8938 dB, SSIM: 0.99446 dB.

To further demonstrate the advantages of the algorithm proposed in this paper in processing closed-loop feature images, Lena image is selected for comparison experiments in this paper, as shown in Figure 17 and Table 3. The image is available in the public and royalty-free database https://ccia.ugr.es/cvg/dbimagenes/index.php. According to the experimental results, it can be found that the results of the algorithm in this paper have lower values compared with the results of processing biological slice images, and have little advantage over other algorithms in processing Lena image, but are generally better.

Figure 17. Denoising results of the Lena image for different values of noise level (see column 1 located on the left side of the figure). The algorithm used, Shearlet method, TV method, Bilateral Filtering, Trilateral Filtering, and Compressed sensing are arranged in columns 2, 3, 4, 5, 6 and 7, respectively.

Table 3. Image denoising effect comparison.

Image	Noise Level	Metrics	Noisy Image	Proposed Method	Shearlet Method	TV Method	Bilateral Filter	Trilateral Filter	CS Method
Lena	10%	PSNR	21.9101	35.0515	35.0492	32.3192	33.6869	33.5642	31.8017
		SSIM	0.60183	0.90414	0.90224	0.85623	0.86098	0.86286	0.80518
	20%	PSNR	19.6038	31.538	32.0515	30.9875	26.4833	28.842	27.5548
		SSIM	0.33727	0.84782	0.8527	0.82726	0.54801	0.67866	0.58548
	30%	PSNR	17.4178	29.3823	30.1649	27.5599	21.203	25.4106	24.4917
		SSIM	0.21635	0.80018	0.81011	0.65659	0.30691	0.51157	0.42964
	80%	PSNR	11.2096	22.3959	24.5949	16.3738	11.7591	16.4136	17.2207
		SSIM	0.06103	0.66531	0.70373	0.15597	0.067922	0.18269	0.15611

5. Conclusions

Aiming at the noise texture in the process of cross-sectional image acquisition, this paper proposes a Bendlet domain adaptive filtering method for denoising biological slice images by combining the image features of locust slices and the latest multi-scale geometric analysis tool Bendlet transform. Bendlet is a second-order shearlet system that can optimally identify image texture information. Compared with classic and newer denoising algorithms, bendlet can effectively repair small image damage, enhance and protect image details, which is currently a more effective image processing tool. In addition, the method proposed in this paper can also be extended to other biological cross-sectional images.

Acknowledgments

This work was supported by the National Natural Science Foundation of China (Grant No. 61871380), Shandong Provincial Natural Science Foundation (Grant No. ZR2020MF019), and Beijing Natural Science Foundation (Grant No. 4172034).

Conflict of interest

The authors declare that there is no conflict of interest.

References

1. Q. Ma, S. Mei, D. Zhu, Application of microscopic image segmentation technology in Locust-Control pesticide research, in *2010 Second International Workshop on Education Technology and Computer Science*, IEEE, **3** (2010), 15–18. https://doi.org/10.1109/ETCS.2010.178
2. L. I. Rudin, S. Osher, E. Fatemi, Nonlinear total variation based noise removal algorithms, *Physica D*, **60** (1992), 259–268.
3. C. Tomasi, R. Manduchi, Bilateral filtering for gray and color images, in *Sixth International Conference on Computer Vision (IEEE Cat. No. 98CH36271)*, (1998), 839–846. https://doi.org/10.1109/ICCV.1998.710815
4. W. C. K. Wong, A. C. S. Chung, S. C. H. Yu, Trilateral filtering for biomedical images, in *2004 2nd IEEE International Symposium on Biomedical Imaging: Nano to Macro (IEEE Cat No. 04EX821)*, (2004), 820–823. https://doi.org/10.1109/ISBI.2004.1398664
5. A. E. Mahdaoui, A. Ouahabi, M. S. Moulay, Image denoising using a compressive sensing approach based on regularization constraints, *Sensors*, **22** (2022), 2199. https://doi.org/10.3390/s22062199
6. A. Buades, B. Coll, J. M. Morel, A review of image denoising algorithms, with a new one, *Multiscale Model. Simul.*, **4** (2005), 490–530. https://doi.org/10.1137/040616024
7. J. Froment, Parameter-free fast pixelwise non-local means denoising, *Image Process. On Line*, **4** (2014), 300–326. https://doi.org/10.5201/ipol.2014.120

8. P. Zhang, Y. Liu, Z. Gui, Y. Chen, L. Jia, A region-adaptive non-local denoising algorithm for low-dose computed tomography images, *Math. Biosci. Eng.*, **20** (2023), 2831–2846. https://doi.org/10.3934/mbe.2023133

9. Y. Hou, C. Zhao, D. Yang, Y. Cheng, "Comments on" image denoising by sparse 3-D transform-domain collaborative filtering, *IEEE Trans. Image Process.*, **20** (2010), 268–270. https://doi.org/10.1109/TIP.2010.2052281

10. H. Yin, Y. Gong, G. Qiu, Side window filtering, in *Proceedings of the IEEE/CVF Conference on Computer Vision and Pattern Recognition*, (2019), 8758–8766.

11. K. Simonyan, A. Zisserman, Very deep convolutional networks for large-scale image recognition, preprint, arXiv:1409.1556. https://doi.org/10.48550/arXiv.1409.1556

12. C. Szegedy, W. Liu, Y. Jia, P. Sermanet, S. Reed, D. Anguelov, et al., Going deeper with convolutions, in *Proceedings of the IEEE Conference on Computer Vision and Pattern Recognition (CVPR)*, 2015.

13. S. Anwar, N. Barnes, Real image denoising with feature attention, in *Proceedings of the IEEE/CVF International Conference on Computer Vision (ICCV)*, (2019), 3155–3164.

14. Y. Zhang, Y. Tian, Y. Kong, B. Zhong, Y. Fu, Residual dense network for image restoration, *IEEE Trans. Pattern Anal. Mach. Intell.*, **43** (2020), 2480–2495. https://doi.org/10.1109/TPAMI.2020.2968521

15. P. Isola, J. Zhu, T. Zhou, A. Efros, Image-to-image translation with conditional adversarial networks, in *Proceedings of the IEEE Conference on Computer Vision and Pattern Recognition (CVPR)*, (2017), 1125–1134.

16. D. Valsesia, G. Fracastoro, E. Magli, Deep graph-convolutional image denoising, *IEEE Trans. Image Process.*, **29** (2020), 8226–8237. https://doi.org/10.1109/TIP.2020.3013166

17. O. Moussa, N. Khlifa, F. Morain-Nicolier, An effective shearlet-based anisotropic diffusion technique for despeckling ultrasound medical images, *Multimedia Tools Appl.*, **2022** (2022), 1–24. https://doi.org/10.1007/s11042-022-13642-0

18. K. Rao, M. Bansal, G. Kaur, An effective CT medical image enhancement system based on DT-CWT and adaptable morphology, *Circuits Syst. Signal Process.*, **2022** (2022), 1–29. https://doi.org/10.1007/s00034-022-02163-8

19. W. El-Shafai, A. Mahmoud, A. Ali, E. S. El-Rabaie, T. Taha, O. Zahran, et al., Deep CNN model for multimodal medical image denoising, *Comput. Mater. Contin.*, **73** (2022), 3795–3814. https://doi.org/10.32604/cmc.2022.029134

20. X. Jia, D. Meng, X. Zhang, X. Feng, PDNet: Progressive denoising network via stochastic supervision on reaction-diffusion–advection equation, *Inf. Sci.*, **610** (2022), 345–358. https://doi.org/https://doi.org/10.1016/j.ins.2022.07.138

21. J. Mazloum, S. M. Hadian, A time-splitting local meshfree approach for time-fractional anisotropic diffusion equation: application in image denoising, *Adv. Contin. Discrete Models*, **2022** (2022), 1–19. https://doi.org/10.1186/s13662-022-03728-2

22. S. Mei, M. Liu, A. Kudreyko, P. Cattani, D. Baikov, F. Villecco, Bendlet transform based adaptive denoising method for microsection images, *Entropy*, **24** (2022), 869. https://doi.org/10.3390/e24070869

23. S. Gai, Multichannel image denoising using color monogenic curvelet transform, *Soft Comput.*, **22** (2018), 635–644. https://doi.org/10.1007/s00500-016-2361-1

24. Y. Zhang, Y. Wei, S. Mei, M. Zhu, Application of multi-scale interval interpolation wavelet in beef image of marbling segmentation, *Trans. Chin. Soc. Agric. Eng.*, **32** (2016), 296–304.

25. D. L. Donoho, Wedgelets: Nearly minimax estimation of edges, *Ann. Stat.*, **27** (1999), 859–897.

26. H. S. Jung, M. H. Sunwoo, Texture-based block partitioning method for motion compensated frame interpolation, *SpringerPlus*, **5** (2016), 1–17. https://doi.org/10.1186/s40064-016-3504-7

27. D. L. Donoho, X. Huo, Beamlets and multiscale image analysis, *Multiscale Multiresolution Methods*, **2002** (2002), 149–196.

28. B. Hou, F. Liu, L. Jiao, Linear feature detection based on ridgelet, *Sci. China Ser. E: Technol. Sci.*, **46** (2003), 141–152. https://doi.org/10.1360/03ye9015

29. E. J. Candes, D. L. Donoho, *Curvelets: A Surprisingly Effective Nonadaptive Representation for Objects with Edges*, Stanford University, 2000.

30. M. Arif, G. Wang, Fast curvelet transform through genetic algorithm for multimodal medical image fusion, *Soft Comput.*, **24** (2020), 1815–1836. https://doi.org/10.1007/s00500-019-04011-5

31. E. Le Pennec, S. Mallat, Image compression with geometrical wavelets, in *Proceedings 2000 International Conference on Image Processing (Cat. No. 00CH37101)*, **1** (2000), 661–664. https://doi.org/10.1109/ICIP.2000.901045

32. E. Le Pennec, S. Mallat, Sparse geometric image representations with bandelets, *IEEE Trans. Image Process.*, **14** (2005), 423–438. https://doi.org/10.1109/TIP.2005.843753

33. M. N. Do, M. Vetterli, The contourlet transform: an efficient directional multiresolution image representation, *IEEE Trans. Image Process.*, **14** (2005), 2091–2106. https://doi.org/10.1109/TIP.2005.859376

34. G. Kutyniok, W. Q. Lim, R. Reisenhofer, Shearlab 3D: Faithful digital shearlet transforms based on compactly supported shearlets, *ACM Trans. Math. Software*, **42** (2016), 1–42. https://doi.org/10.1145/2740960

35. S. Alinsaif, J. Lang, Texture features in the Shearlet domain for histopathological image classification, *BMC Med. Inf. Decis. Making*, **20** (2020), 1–19. https://doi.org/10.1186/s12911-020-01327-3

36. C. Lessig, P. Petersen, M. Schäfer, Bendlets: A second-order shearlet transform with bent elements, *Appl. Comput. Harmon. Anal.*, **46** (2019), 384–399. https://doi.org/10.1016/j.acha.2017.06.002

37. S. Poovizhi, T. R. G. Babu, R. Praveena, Certain investigations on melanoma detection using nonsubsampled bendlet transform with different classifiers, *Mol. Cell. Biomech.*, **18** (2021), 201–219. https://doi.org/10.32604/mcb.2021.017984

38. A. Maalouf, P. Carre, B. Augereau, C. Fernandez-Maloigne, A bandelet-based inpainting technique for clouds removal from remotely sensed images, *IEEE Trans. Geosci. Remote Sens.*, **47** (2009), 2363–2371. https://doi.org/10.1109/TGRS.2008.2010454

39. M. Ferroukhi, A. Ouahabi, M. Attari, Y. Habchi, A. Taleb-Ahmed, Medical video coding based on 2nd-generation wavelets: performance evaluation, *Electronics*, **8** (2019), 88. https://doi.org/10.3390/electronics8010088

40. H. Wang, M. Zhu, L. Li, L. Wang, H. Zhao, S. Mei, Regional weed identification method from wheat field based on unmanned aerial vehicle image and shearlets, *Trans. Chin. Soc. Agric. Eng.*, **33** (2017), 99–106.

41. T. Fink, Higher order analysis of the geometry of singularities using the Taylorlet transform, *Adv. Comput. Math.*, **45** (2019), 675–705. https://doi.org/10.1007/s10444-018-9635-3

42. H. Wang, J. Liu, L. Liu, M. Zhao, S. Mei, Coupling technology of OpenSURF and Shannon-Cosine wavelet interpolation for locust slice images inpainting, *Comput. Electron. Agric.*, **198** (2022), 107110. https://doi.org/10.1016/j.compag.2022.107110

43. S. Mei, W. Gao, Shannon-Cosine wavelet spectral method for solving fractional Fokker–Planck equations, *Int. J. Wavelets Multiresolution Inf. Process.*, **16** (2018), 1850021. https://doi.org/10.1142/S0219691318500212

44. L. Liu, M. Liu, K. Meng, L. Yang, M. Zhao, S. Mei, Camouflaged locust segmentation based on PraNet, *Comput. Electron. Agric.*, **198** (2022), 107061. https://doi.org/10.1016/j.compag.2022.107061

45. T. R. Ganesh Babu, An efficient skin cancer diagnostic system using Bendlet Transform and support vector machine, *Anais da Academia Brasileira de Ciências*, **92** (2020), 1–12. https://doi.org/10.1590/0001-3765202020190554

46. R. Kushol, M. H. Kabir, M. Abdullah-Al-Wadud, M. S. Islam, Retinal blood vessel segmentation from fundus image using an efficient multiscale directional representation technique Bendlets, *Math. Biosci. Eng.*, **17** (2020), 7751–7771. https://doi.org/10.3934/mbe.2020394

47. S. Mei, K. Chen, S. Zhang, Quasi Shannon wavelet numerical solution of two-point boundary value problems, *J. China Agric. Univ.*, **7** (2002), 12–16.

48. D. L. Donoho, De-noising by soft-thresholding, *IEEE Trans. Inf. Theory*, **41** (1995), 613–627. https://doi.org/10.1109/18.382009

49. A. Ouahabi, A review of wavelet denoising in medical imaging, in *2013 8th International Workshop on Systems, Signal Processing and Their Applications (WoSSPA)*, (2013), 19–26. https://doi.org/10.1109/WoSSPA.2013.6602330

50. A. M. Atto, Y. Berthoumieu, Wavelet packets of nonstationary random processes: Contributing factors for stationarity and decorrelation, *IEEE Trans. Inf. Theory*, **58** (2011), 317–330. https://doi.org/10.1109/TIT.2011.2167496

51. R. Abazari, M. Lakestani, A hybrid denoising algorithm based on shearlet transform method and Yaroslavsky's filter, *Multimedia Tools Appl.*, **77** (2018), 17829–17851. https://doi.org/10.1007/s11042-018-5648-7

52. Z. Mousavi, M. Lakestani, M. Razzaghi, Combined shearlet shrinkage and total variation minimization for image denoising, *Iran. J. Sci. Technol. Trans. A: Sci.*, **42** (2018), 31–37. https://doi.org/10.1007/s40995-017-0327-5

AIMS Press